Journal of
Manufacturing and Materials Processing

MDPI

Article

Stainless Steel 316L Fabricated by Fused Deposition Modeling Process: Microstructure, Geometrical and Mechanical Properties

Maria Zaitceva *, Anton Sotov, Anatoliy Popovich and Vadim Sufiiarov

Institute of Mechanical Engineering, Materials, and Transport, Peter the Great St. Petersburg Polytechnic University, Polytechnicheskaya, 29, 195251 St. Petersburg, Russia
* Correspondence: zajtsevamya@yandex.ru

Abstract: Additive manufacturing (AM) methods are widely used to produce metal products. However, the cost of equipment for processes based on material melting is high. In this paper, a promising, less expensive method of producing metal products from metal-filled Ultrafuse 316L filament by FDM was investigated. The aim of this work was to compare the debinding methods and investigate the microstructure, phase composition, and geometric and mechanical properties. The results showed that catalytic debinding can be replaced by thermal debinding as no significant effect on the structure and properties was found. In addition, a filament study was performed and data on the particle size distribution, morphology, and phase composition of the metal particles were obtained. Thermodynamic modeling was performed to better understand the phase distribution at the sintering stage. The δ-Fe fraction influencing the corrosion properties of the material was estimated. The conformity of geometric dimensions to the original 3D models was evaluated using 3D scanning. The applied printing and post-processing parameters allowed us to obtain a density of 98%. The material and technology represent a promising direction for applications in the field of lightweight engineering in the manufacturing of parts with bioinspired designs, shells, and sparse filler structures with useful porosity designs (like helicoidal structures).

Keywords: additive manufacturing; material extrusion; fused deposition modeling; sintering; stainless steel; helicoidal structure; 3D printing

Citation: Zaitceva, M.; Sotov, A.; Popovich, A.; Sufiiarov, V. Stainless Steel 316L Fabricated by Fused Deposition Modeling Process: Microstructure, Geometrical and Mechanical Properties. *J. Manuf. Mater. Process.* **2024**, *8*, 259. https://doi.org/10.3390/jmmp8060259

Academic Editor: Steven Y. Liang

Received: 8 October 2024
Revised: 7 November 2024
Accepted: 12 November 2024
Published: 14 November 2024

1. Introduction

Additive manufacturing represents a significant and dynamic field of production, driven by the speed and adaptability of the process and the capacity to manufacture products of intricate geometry, which are challenging to produce through traditional techniques [1–3].

The most common raw materials used for additive manufacturing of metals are metal powders [4,5], which require high-energy sources for their fusion. The application of these technologies is constrained to areas where a substantial initial investment in equipment and the assurance of safe operation would be economically justifiable. In most cases, the formation of the product occurs when the metal is heated to its melting point, resulting in significant structural and phase changes that allow for the formation of large residual stresses and defects associated with high cooling rates.

The manufacturing of metal products using metal-filled filaments has become increasingly popular in recent years, as it allows for a reduction in production costs through the use of common low-cost 3D printers based on the material extrusion process and using outsourced services for post-processing at specialized companies. The most popular technology for this process is fused deposition modeling (FDM). The growing interest in the manufacturing of metal products by material extrusion is, among other factors, due to the ability to create small items with different internal fillings, which significantly reduces their weight. The technology does not necessitate the creation of special channels or outlets for

the removal of excess powder from the internal cavities. The limitations of the modeling process are the minimum allowable wall thickness, the necessity of at least one flat plane for post-processing and for the employment of supporting structures for overhanging geometries, the size of the printer work platform and the necessity of a postprocessing furnace. The principal disadvantages of this process are the porosity and anisotropy of the items produced, which have a detrimental impact on the mechanical properties.

The most used and extensively studied filaments for the FDM metal printing are those containing particles of stainless steel, specifically SS316L and SS17-4PH. The use of copper [6], titanium [7] and nickel alloys [8] is less common, although these materials have great potential from a scientific and technological standpoint. Several commercial metal-filled filaments are popular for research, including those produced by BASF, Virtual Foundries, Desktop Metals [9,10] and Markforged [11]. These companies are well-known manufacturers of raw material for metal injection molding technologies (MIM) [2], and some studies focus on the development of material extrusion with them [12–14].

Austenitic 316L stainless steel has already been the subject of extensive research and is employed in a multitude of industrial contexts, which can be attributed to its favorable balance of cost, corrosion resistance, ductility, strength properties, and machinability. The alloy is employed in the production of orthopedic implants [15], equipment for oil refining and nuclear power engineering, heat exchangers, and other applications [16].

The process of 3D printing with metal-filled filament consists of three main stages: 3D printing (green model), removal of the binder (brown model) and sintering (sintered part). The binder removal stage is influenced by two factors: the type of binder (soluble, catalytically removable, burnable or a combination of these) and the temperature mode of debinding. Most used binders have complex compositions; therefore, their removal is conducted in two stages. At the first, the main component (50–90 vol.%) is dissolved. Then, components responsible for shape retention (0–50 vol.%) and various additives as stabilizers and dispersing agents (0–10 vol.%) are burned out.

After the binder is removed, sintering takes place, during which atomic diffusion occurs between the metal particles. At this stage, the product attains its final density. The sintering temperature is typically 70–90% of the melting point of the material [17]. The binder burning and sintering stages are carried out sequentially and continuously and are usually carried out in the same furnace due to the high brittleness of brown models. It is of the utmost importance to select heat treatment parameters with great care, as defects such as pores and cracks and various types of delamination and warpage may occur during the binder removal and sintering stages.

A significant amount of research on FDM with metal-filled filaments of 316L stainless steel has been dedicated to the optimization of the printing process, assessing the mechanical properties of the material and reducing porosity [18–31]. Tosto et al. explored methods for enhancing the density of green models, resulting in tensile properties that are comparable with MIM ones [23]. Prior research has demonstrated that porosity has a considerable impact on mechanical properties [24,25]. The mechanical characteristics are also influenced by the infill density [26]. The findings of the study conducted by Ait-Mansour et al. [27] indicate a linear correlation between infill density and mechanical strength. The results of research carried out by Kasha et al. [28] showed that the printing orientation affects the flexural characteristics, and the best results were obtained when the samples were manufactured 'on-edge'. The tensile, compression and flexural properties and hardness of the SS316L material were evaluated by Carminati et al. [29]. Additionally, the tensile properties of the material were assessed in the study by Spiller et al. [30]. A comparative analysis of the tensile properties of samples of 316L stainless steel produced by FDM with metal-filled filament via catalytic debinding in a laboratory setting at 80 °C and in industrial facilities (BASF and Vibrom companies), as well as those produced by the selective laser melting (SLM) method, was conducted [31].

It may be more reasonable to consider FDM with metal-filled filaments as a technology distinct from those such as powder bed fusion (PBF) and direct energy deposition (DED),

rather than as a direct competitor. One of the principal advantages of DED-based technologies is the ability to produce items of considerable dimensions [32,33]. Consequently, PBF-based technologies enable the manufacture of products with intricate geometries with a high degree of accuracy [34,35]. Furthermore, the technology enables one to obtain the mechanical properties at the level of bulk materials [36]. Comparative studies have demonstrated that the mechanical properties of parts manufactured using metal-filled filaments are lower than those produced by laser-based PBF (L-PBF) [37,38]. Nevertheless, the production cost of L-PBF is approximately 4.5 times higher than FDM with metal-filled filament [39]. In addition, the cost of sintering equipment is still lower than printers using other metal additive manufacturing technologies.

The use of metal-filled filament and FDM has the potential to be applied in the field of lightweight engineering for the production of parts with bioinspired designs, shells, sparse filler structures with predetermined useful porosities (such as for helicoidal structures) and damping components for improved compression and energy dissipation properties during deformation.

Such products include bioinspired structures, in particular the helicoidal structure. This structure is formed by successive stacking of fiber layers in such a way that the centers of the axes of fibers with the same serial number within a layer form a helical line [40–42]. This structure has several manifestations in nature: the exoskeleton of crabs and lobsters [43,44], the elytra of beetles [45], and the hammer-like claw of the mantis shrimp [46]. Helicoidal structures can be manufactured from a variety of materials, including stainless steel.

Notwithstanding the considerable amount of research that has been conducted and published on this topic, the majority of studies do not investigate the debinding step, as the products are outsourced for post-processing. Given the complexity of catalytic debinding, which necessitates the use of expensive equipment, it is of interest to ascertain the feasibility of undertaking an alternative type of post-treatment, namely thermal debinding, and to conduct a comparative analysis of the resulting properties. Despite its extensive use in numerous studies, Ultrafuse 316L filament has not been subjected to sufficient investigations. Given the considerable impact of the initial material in determining the final properties of the products, an in-depth examination of characteristics such as the size and morphology of metal particles and their distribution within the binder, along with their phase composition, is imperative. In addition, as one of the steps is sintering, it is essential to examine the specific characteristics of phase composition formation, with particular attention paid to δ-Fe, since the quantity of this phase affects corrosion resistance.

The present article aims to investigate Ultrafuse 316L filament, compare debinding methods and their influence on the final properties, and establish the features of structure formation, phase composition and geometric accuracy after the full cycle of additive manufacturing. Furthermore, it will facilitate the identification of avenues for enhancing technological processes and potential applications, with a particular focus on the microstructural features, properties and geometrical characteristics that can be achieved. This study serves as a foundation for subsequent investigations, which will aim to explore the specific characteristics of manufacturing products with complex geometries, including helicoidal structures.

2. Materials and Methods

Commercial BASF Ultrafuse 316L filament with 1.75 mm diameter was used for 3D printing. Table 1 presents the typical chemical composition for the selected filament. According to the manufacturer's data [47], the density of the material after sintering is 7.85 g/cm^3. It must be taken into account that the density and chemical composition depend on the atmosphere and the processing temperature at each stage.

Table 1. Standard chemical composition after sintering [47].

C, %	Cr, %	Ni, %	Mn, %	Mo, %	Si, %	Fe, %
≤0.03	16–18	10–14	≤2	2–3	≤1	bal.

2.1. Green Model Fabrication

Three-dimensional printing was carried out using an Anisoprint Composer A4 desktop printer which has a maximum platform heating temperature of up to 120 °C (when the chamber is open). The selected 3D printer was coupled with its proprietary Aura Slicer for the processing of the geometry. The printing parameters are shown in Table 2. The print pattern consisted of three perimeters and an internal zigzag filling with a 45° change in direction on each layer. Shrinkage (XY ~ 16%, Z ~ 20%) and corresponding scaling factors were considered during the design of the initial 3D models, using the manufacturer's recommended formulae [48]. For investigation of printing, post-processing and microstructure analysis, a series of cubic-shaped specimens with dimensions of 10 × 10 × 10 mm, as well as flat dog bone specimens for mechanical tests, were manufactured. Additionally, several complex-shaped objects used for the estimation of geometrical features were fabricated.

Table 2. Printing parameters.

Parameter	Value
Nozzle temperature	245 °C
Bed temperature (5 layers)	105 °C
Bed temperature	90 °C
Layer thickness	0.1 mm; 0.2 mm
Extrusion coefficient	105%
Hatch distance	0.5 mm
Printing speed	25 mm/s
Diameter of nozzle	0.5 mm

2.2. Debinding and Sintering Processes

The catalytic binder removal process was carried out in a specially constructed laboratory device (Figure 1). The device consists of a furnace equipped with a heating element, thermocouples to control the heating temperature, an inert gas supply system and a gas burner to burn the reaction products. Samples in crucibles and a container of high-purity nitric acid were placed inside the furnace. The process was carried out at 120 °C and conducted under argon blowing-off conditions. The holding time was chosen as a rate of 2 mm/h for each external surface. A propane connection was established to a gas burner, which was then used to incinerate the reaction products.

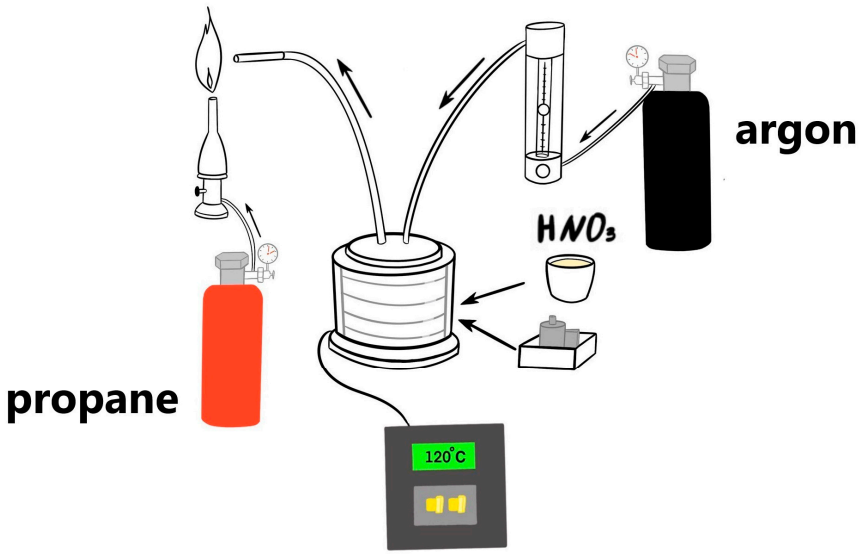

Figure 1. Scheme of catalytic debinding.

For thermal debinding and sintering, a Carbolite Gero LHTW 200-300/22-1G (Carbolite Gero Ltd., Derbyshire, UK) furnace was used. To burn out the binder, the samples were slowly heated up to 400 °C and held for 3 h, and then temperature was raised to 600 °C and held for 1 h. After this process, the samples were sintered at 1380 °C for 3 h.

A schematic representation of the entire production process is provided in Figure 2.

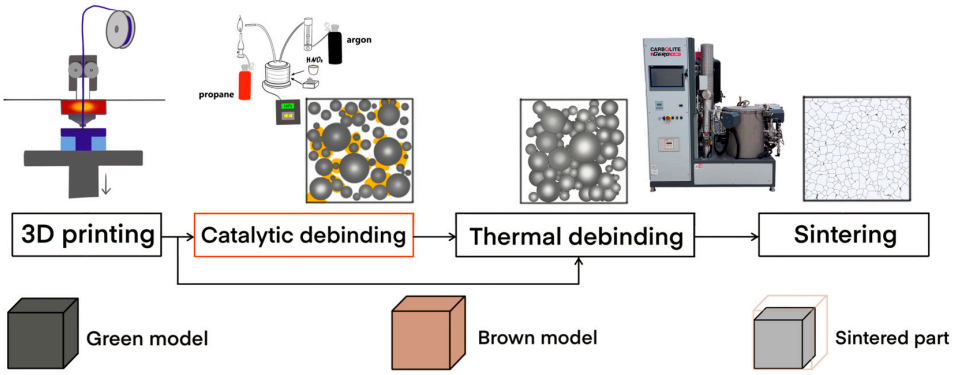

Figure 2. Process line of FDM additive manufacturing with metal-filled filament.

2.3. Characterization

Density was measured using the Archimedes method. Differential scanning calorimetry (DSC) analysis of the filament was performed on a NETZSCH DSC 404 F3 calorimeter (NETZSCH GmbH, Selb, Germany) at a heating rate of 3 °C/min in an argon protective atmosphere. The particle size distribution of the metal powder after binder removal was measured using a Fritsch Analysette 22 NanoTec plus laser diffractometer (Fritsch GmbH, Idar-Oberstein, Germany).

The macrostructure of the samples was studied using a Leica DMI 5000 optical microscope and a Tescan Mira3 LMU scanning electron microscope. To reveal the structural components, the samples were etched in the following solution: $FeCl_3$ (100 mg), C_2H_5OH (10 mL), HCl (10 mL) and HNO_3 (10 mL).

The main characteristics of the phase structure of the samples were analyzed using a Bruker D8 Advance X-ray diffractometer (XRD). Cu Kα radiation (λ = 1.5406 Å) with a scanning interval of 0.02° was used. Tensile and compression tests were performed on a Zwick/Roell Z100 universal testing machine at 20 °C with a 100 kN load cell. For these tests, type 1 samples were made in accordance with ISO 6892-1:2019 "Metallic materials—Tensile testing—Part 1: Method of test at room temperature" [49]. Flat dog bone specimens were built horizontally (XY). Microhardness was measured on a Buehler VH1150 hardness tester at a load of 100 g. Cubic samples were employed for the purposes of conducting macro- and microstructure studies, as well as phase analysis and microhardness measurements.

Thermodynamic modeling was performed using the JMatPro version 7 software to better understand the influence of the selected sintering temperature on the phase transformations: Gibbs energy, phase composition and phase fractions were estimated.

For 3D scanning, a Shining EinScan-SE 3D scanner (SHINING 3D Tech Co., Ltd, Hangzhou, China) was used. The geometric dimensions of the green model were compared to the dimensions of the 3D model after scaling, and the dimensions of the sintered parts were compared to those of the original models.

3. Results and Discussion

3.1. Ultrafuse 316L Filament

In the first stage, an initial metal-filled filament with a density of 4.75 g/cm^3 was investigated. The filament consists of spherical metal particles in a binder and a polymer shell with a thickness of 58–78 µm (Figure 3a,b). The metal particles are uniformly distributed throughout the inner volume. The internal porosity of the powder was identified (Figure 3e).

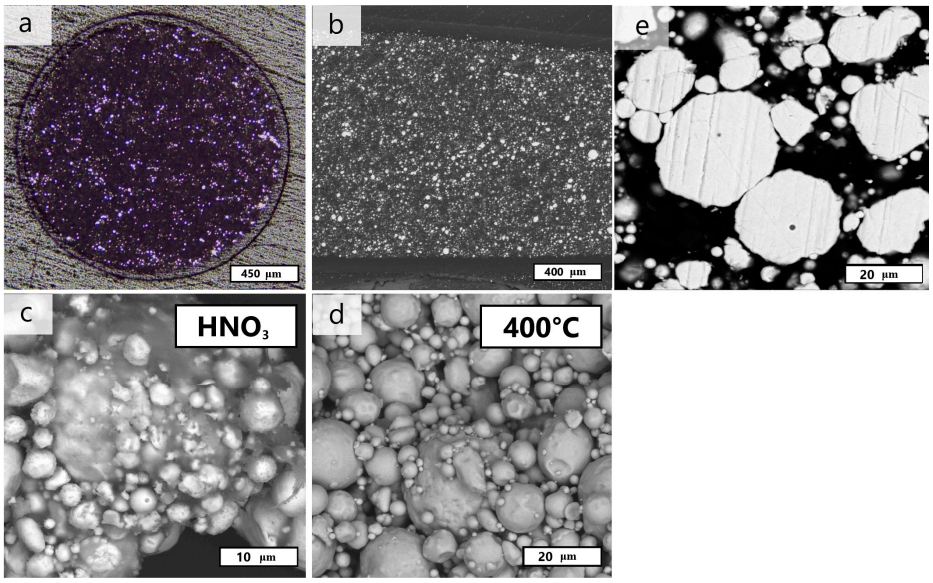

Figure 3. Images of filament: (**a**) cross section, (**b**) longitudinal section; metal particles after (**c**) removal of binder in nitric acid, (**d**) thermal debinding, (**e**) powder cross section.

After the removal of the binder by the two methods—catalysis in nitric acid vapor and burning at 400 °C—it was found that the binder consists of two components, one of which requires thermal decomposition (Figure 3c). The metal particles were presumably obtained by gas atomization [50], as evidenced by the spherical shape of the particles and the presence of pores on the surface of the particles. Metal powder particles have the following particle size distribution: d10 = 5.7 µm, d50 = 14.5 µm, d90 = 28.1 µm. A particle size distribution similar to the one obtained is used in the manufacturing of metal products by MIM and binder jetting [51]. Two peaks are observed on the obtained DSC curve at temperatures of 107 °C and 166 °C (Figure 4). The first peak corresponds to the crystallization temperature and the second to the melting point. These results were used to select the operating temperatures for the build platform and nozzle heating.

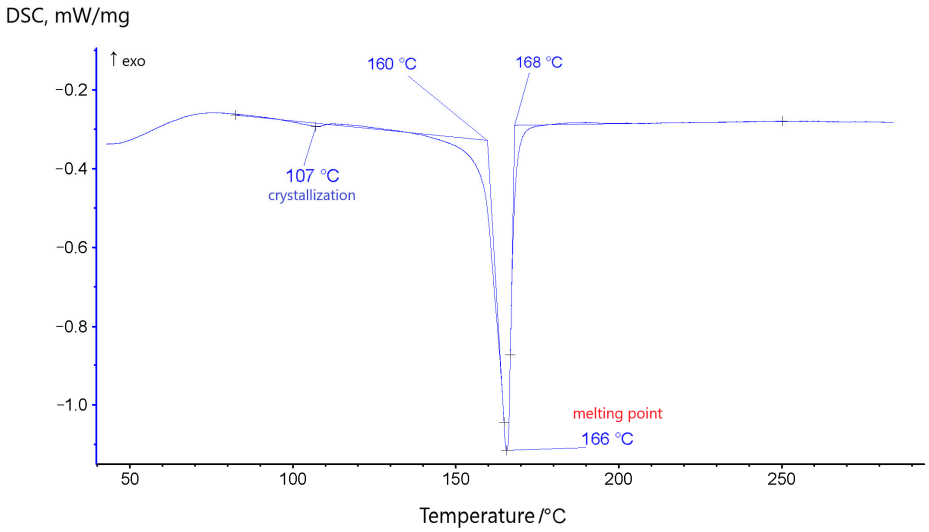

Figure 4. DSC curve of filament.

3.2. Printing and Post-Processing

To ensure the necessary adhesion of the samples, the build platform was heated to 105 °C for the first five layers and then cooled down to 90 °C. The quality of the material extrusion was determined by visual inspection, and it was determined that with a flow

ratio of 105%, there was sufficient adhesion between the layers and no over-extrusion of the material, as evidenced by the quality of the surface layer and the geometric dimensions of the samples. The appearances of the samples at all stages of the manufacturing process are shown in Figure 5.

Figure 5. Sample appearance at the production stages.

Figure 6 shows images of the macrostructure of the green models and sintered parts. The average shrinkage of the samples along the axes was X—16.8%, Y—17%, Z—19.5%. In all specimens, internal voids were found at the junction of the outer perimeters and the filling, as well as at the nozzle turns. After sintering, no metallic bonds were formed in these areas due to the insufficient amount of metallic particles. Based on the sintering results, it was concluded that the sample with a lower layer thickness is less prone to internal void formation due to improved adhesion between layers. The highest density measured was 7.7 g/cm^3 (98%), and it was obtained for the samples printed with a layer thickness of 0.1 mm. Hot isostatic pressing may be used as a possible method to increase the density of the material and to reduce the volume and size of defects [52].

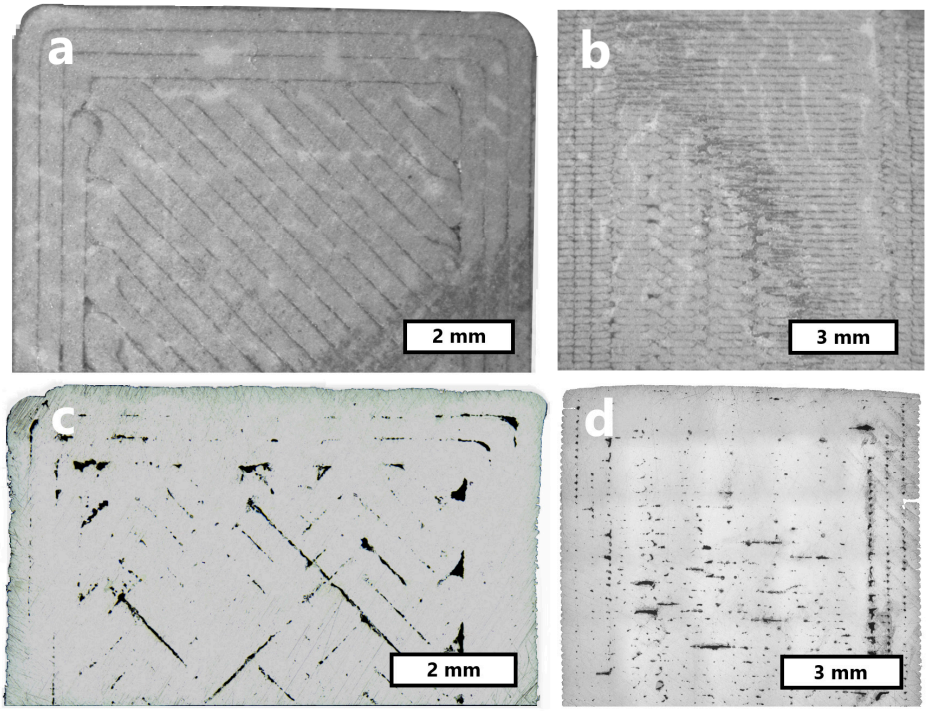

Figure 6. Cross sections of 3D-printed samples: (**a**,**b**) green models, (**c**,**d**) sintered parts.

3.3. Microstructural Analysis

XRD analyses of the metal filament particles and samples after the debinding by the two methods and subsequent sintering were carried out (Figure 7). The presence of peaks 2θ = 43°, 53° and 74° corresponding to the FCC lattice of γ-Fe and 2θ = 44°, 65° and 81° corresponding to the BCC lattice of δ-Fe were detected. γ-Fe is the dominant phase in all

samples. The presence of δ-Fe in powder may be explained due to the high cooling rate during gas atomization. A similar reason may explain why no full transformation of δ-Fe to austenite happened during cooling after sintering at 1380 °C [53]. No significant influence of the debinding method on the obtained structure and phase composition was observed.

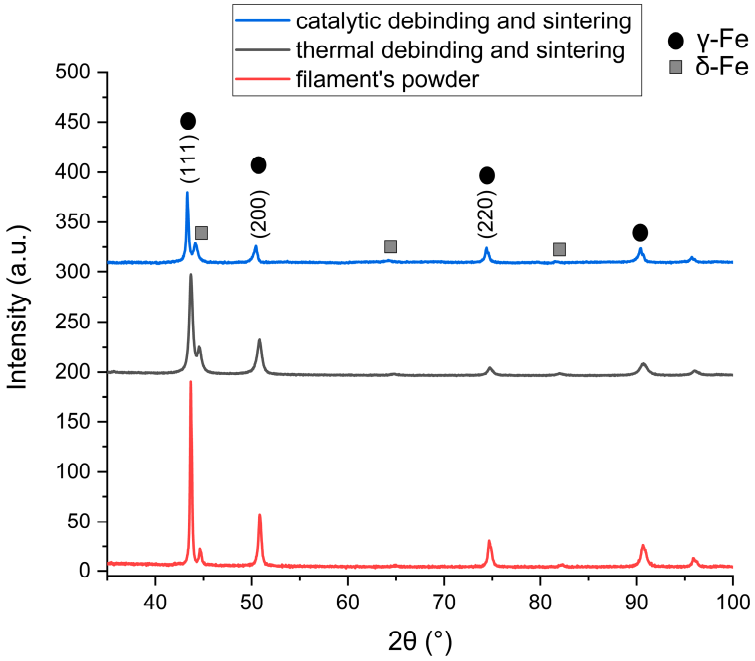

Figure 7. The XRD patterns of samples.

The microstructure obtained after sintering represents equiaxed γ-Fe grains without a pronounced dependence on the direction of 3D printing (Figure 8), in contrast to the columnar grains of products produced by technologies based on melting [54]. The phase of retained δ-Fe is located at grain boundaries. As the grain size is found to be dependent on the sintering temperature and holding time, it was determined that for the chosen heat treatment, the average grain size obtained was ~55 µm. The volume δ-Fe fraction estimated by the metallographic method was 2.5%.

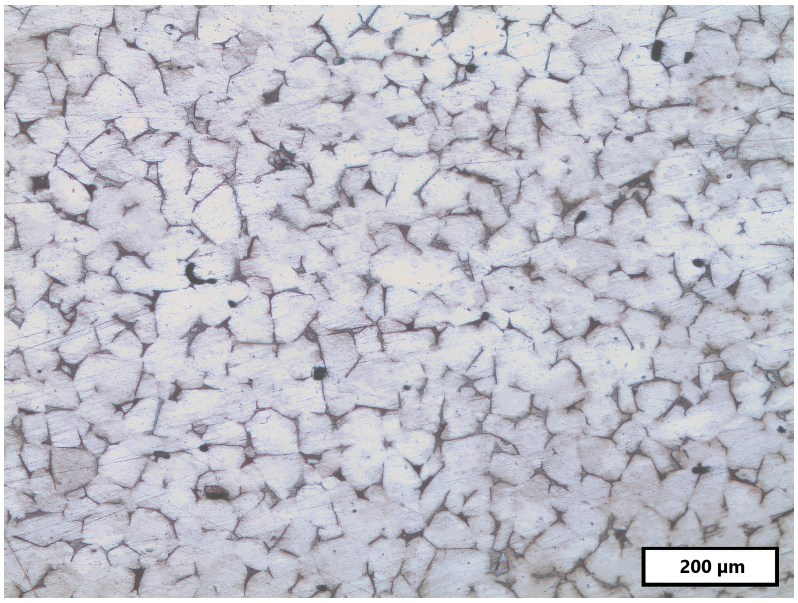

Figure 8. Image of sample microstructure after sintering.

3.4. Mechanical Properties

The average microhardness of the samples after sintering was measured to be 163.7 ± 2.3 HV. The average value of the compressive yield strength was determined at 158.4 ± 14.3 MPa. Table 3 shows a comparison of the obtained tensile mechanical properties with the results of other studies. The yield strength and ultimate strength are close to published data, with a higher value for elongation at the break.

Table 3. Comparison of mechanical properties of SS 316L during tensile tests.

Source	YS, MPa	UTS, MPa	δ, %
Carminati M. et al. [29]	141.9 ± 14.1	426.6 ± 23.7	36.4 ± 3.15
Spiller S. et al. [30]	161	473	37
Kedziora S. et al. [38]	152.9 ± 61.3	314.0 ± 41.7	10.2 ± 5.0
This work	140.8 ± 2.4	455 ± 10.3	38.2 ± 3.6

The data presented in [30] indicate that higher yield and tensile strength values were obtained, which is likely attributable to the lower printing speeds employed. The lower values observed in [38] may be attributed to the influence of different printing parameters and the different building orientation of the tensile specimens. The values obtained in [29] are the most aligned with those presented in this paper; however, the hardness of the samples is lower (132.2 ± 3.8 HV). This difference can be explained by the relatively low nozzle temperature (170 °C), which affected the density of the material (95%).

Nevertheless, the values obtained are markedly lower than those indicated by the manufacturer [47]. The findings indicate that this technology is more suitable for use in applications where the product is not subjected to significant tensile loads. However, it is possible to produce metal products that will have adequate corrosion resistance using this method. Furthermore, it allows one to produce structures with predicted porosity.

3.5. Thermodynamic Modeling

As a result of the thermodynamic modeling, the values of the Gibbs free energy of each phase at different temperatures were obtained. In the temperature range from 1340 °C to 1380 °C the difference in Gibbs free energy of the δ-Fe and γ-Fe phases is close to 0. Consequently, the phase transition in this region has a spontaneous characteristic. During cooling, δ-Fe transforms to γ-Fe. The amount of residual δ-Fe depends on the time and cooling rate of heat treatment. At the sintering temperature, the composition is close to the equilibrium phase content, i.e., the distribution when the percentage of γ-Fe is 66% and δ-Fe is 34%. The amount of δ-Fe can be reduced by introducing step-holding at temperatures of 1000–1200 °C, as an alternative to direct cooling to room temperature, during the cooling phase. This solution should enable one to obtain samples with an γ-Fe structure and will lead to increasing corrosion resistance.

3.6. Complex Part Manufacturing and Comparison of Geometric Dimension

The developed process of manufacturing was applied to produce parts with complex geometries. Figure 9 depicts images of the “bracket”, “helicoidal structure”, “shell” and “cover” parts after 3D printing, thermal debinding and sintering. All items presented were obtained in accordance with the previously outlined set of parameters. This shows that it is possible to use FDM technologies in conjunction with metal-filled filaments for the manufacturing of complex-shaped parts.

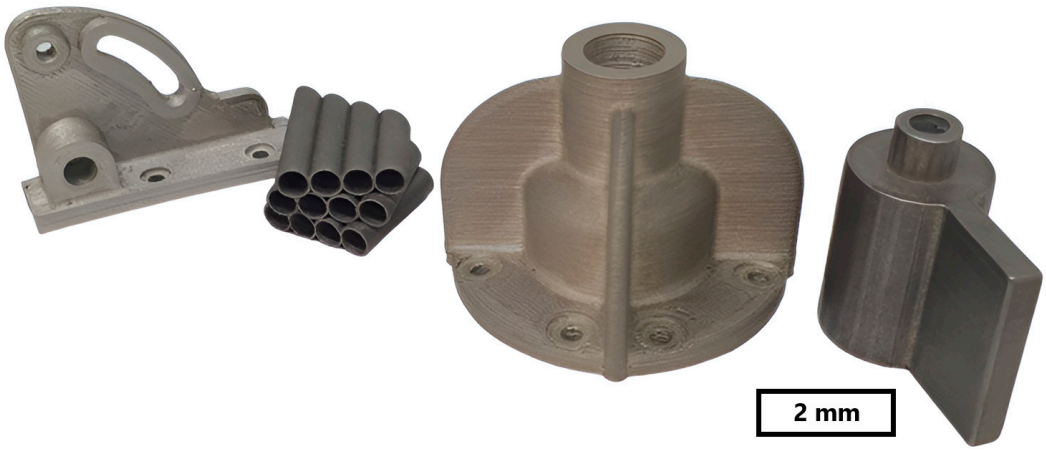

Figure 9. Image of parts manufactured by FDM with metal-filled filament after sintering.

To validate the developed technology of metal-filled filament 3D printing, the dimensions of the geometry "shell" were checked (green model and sintered part). The selected part's geometry comprises a variety of features, including circles, holes, overhanging areas, thin walls and areas with thicker walls. The scanning results showed that the green model matched the 3D model with scale factors (Figure 10a).

The thermal stresses generated during the sintering process caused a slight distortion of the sintered part and a deviation from the original 3D model in the area of thin overhangs (Figure 10b). The average deviation was found to be 160 µm for the green model and 230 µm for the sintered part. The resulting deformations during sintering can be reduced by decreasing the heating and cooling rates.

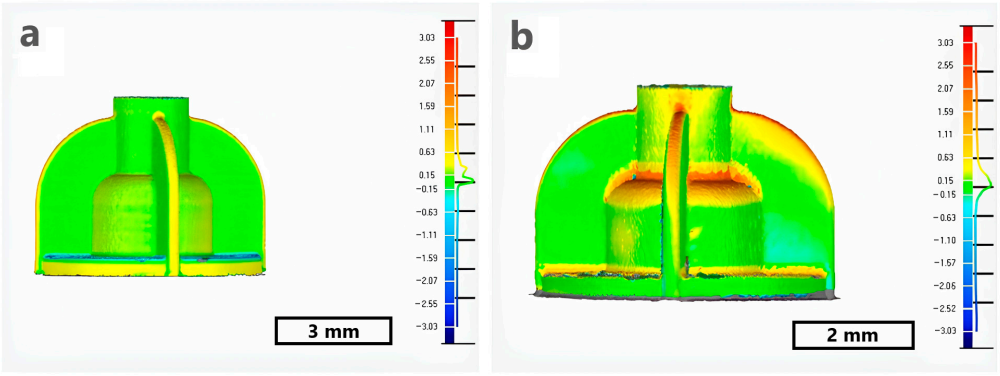

Figure 10. Comparison of geometric dimensions of parts with 3D models: (**a**) green model; (**b**) sintered part.

Although geometry deviations after post-processing are noted, the technology enables us to produce products with sufficiently high accuracy.

4. Conclusions

In the present research, samples were manufactured from metal-filled filament using fused deposition modeling 3D printing with subsequent sintering.

The filament consists of spherical metal particles in a binder and a polymer shell with a thickness of 58–78 µm. Metal powder particles have the following particle size distribution: d10 = 5.7 µm, d50 = 14.5 µm, d90 = 28.1 µm. The presence of pores within the metal particles has been identified as a potential source of concern, as it may lead to an adverse impact on the final density of the products.

The influence of the layer thickness on the resulting macrostructure showed that decreasing the layer thickness enables on to obtain higher densities. The selected printing and post-processing modes enabled a final part density of 98% to be achieved.

The microstructure of the material after sintering consists of γ-Fe and residual δ-Fe, where the average grain size is approximately 55 μm and the value of the δ-Fe is 2.5%.

The measured mechanical properties were tensile yield strength—140.8 ± 2.4 MPa, ultimate tensile strength—455 ± 10.3 MPa, elongation at break—38.2 ± 3.6%, and finally, compressive yield strength—158.4 ± 14.3 MPa.

Several parts with complex geometries have been successfully 3D printed and sintered and subsequently measured by a 3D scanner. The resulting geometry showed an average deviation of 160 μm for the green model and 230 μm for the sintered component, with the most distorted areas located at the areas where thin overhangs are present.

The study revealed that there was no notable distinction in the properties of the material following catalytic and thermal debinding. It can be concluded that the use of thermal debinding instead of catalytic debinding may be employed as an alternative post-processing method if the necessity arises.

In order to enhance corrosion resistance, it is recommended that the sintering mode be adjusted in order to eliminate the δ-Fe fraction. It is therefore proposed that holding at 1000–1200 °C be incorporated as part of the sintering cooling process.

Further investigation is required to enhance the density and strength of the material. This may include studies on the variation in 3D-printing process parameters, an analysis of alternative printing strategies and the application of hot isostatic pressing following sintering.

Author Contributions: V.S.: Conceptualization, Writing—review and editing, supervision, Project administration; M.Z.: Investigation, Data curation, Writing—original draft; A.P.: Funding acquisition, Resources; A.S.: Investigation, Data curation, Writing—review and editing. All authors have read and agreed to the published version of the manuscript.

Funding: This work was funded by the Ministry of Science and Higher Education of the Russian Federation (agreement No. 075-15-2024-562).

Data Availability Statement: The data presented in this study are available on request from the corresponding author.

Conflicts of Interest: The authors declare no conflicts of interest.

References

1. Sufiiarov, V.; Borisov, E.; Polozov, I.; Masaylo, D. Study of microstructure and properties of 316L steel after selective laser melting. In Proceedings of the METAL 2016—25th Anniversary International Conference on Metallurgy and Materials, Brno, Czech Republic, 25–27 May 2016; pp. 659–663.
2. Ramazani, H.; Kami, A. Metal FDM, a new extrusion-based additive manufacturing technology for manufacturing of metallic parts: A review. *Prog. Addit. Manuf.* **2022**, *7*, 609–626. [CrossRef]
3. Nelson, A.T. Prospects for additive manufacturing of nuclear fuel forms. *Prog. Nucl. Energy* **2023**, *155*, 104493. [CrossRef]
4. Sufiiarov, V.; Popovich, A.; Borisov, E.; Polozov, I. Layer thickness influence on the Inconel 718 alloy microstructure and properties under selective laser melting. *Tsvetnye Met.* **2016**, *1*, 81–86. [CrossRef]
5. Sufiiarov, V.; Polozov, I.; Kantykov, A.; Khaidorov, A. Binder jetting additive manufacturing of 420 stainless steel: Densification during sintering and effect of heat treatment on microstructure and hardness. *Mater. Today Proc.* **2019**, *30*, 592–595. [CrossRef]
6. Ren, L.; Zhou, X.; Song, Z.; Zhao, C.; Liu, Q.; Xue, J.; Li, X. Process parameter optimization of extrusion-based 3D metal printing utilizing PW-LDPE-SA binder system. *Materials* **2017**, *10*, 305. [CrossRef]
7. Zhang, Y.; Bai, S.; Riede, M.; Garratt, E.; Roch, A. A comprehensive study on fused filament fabrication of Ti-6Al-4V structures. *Addit. Manuf.* **2020**, *34*, 101256. [CrossRef]
8. Hasib, A.G.; Niauzorau, S.; Xu, W.; Niverty, S.; Kublik, N.; Williams, J.; Chawla, N.; Song, K.; Azeredo, B. Rheology scaling of spherical metal powders dispersed in thermoplastics and its correlation to the extrudability of filaments for 3D printing. *Addit. Manuf.* **2021**, *41*, 101967. [CrossRef]
9. Santamaria, R.; Salasi, M.; Bakhtiari, S.; Leadbeater, G.; Iannuzzi, M.; Quadir, M.Z. Microstructure and mechanical behaviour of 316L stainless steel produced using sinter-based extrusion additive manufacturing. *J. Mater. Sci.* **2022**, *57*, 9646–9662. [CrossRef]

10. Watson, A.; Belding, J.; Ellis, B.D. Characterization of 17-4 PH Processed via Bound Metal Deposition (BMD). In *Proceedings of the TMS 2020 149th Annual Meeting & Exhibition Supplemental Proceedings, San Diego, CA, USA, 23–27 February 2020*; The Minerals, Metals & Materials Series 2020; Springer: Cham, Switzerland, 2020. [CrossRef]
11. Galati, M.; Minetola, P. Analysis of Density, Roughness, and Accuracy of the Atomic Diffusion Additive Manufacturing (ADAM) Process for Metal Parts. *Materials* **2019**, *12*, 4122. [CrossRef]
12. Wagner, M.A.; Hadian, A.; Sebastian, T.; Clemens, F.; Schweizer, T.; Rodriguez-Arbaizar, M.; Carreño-Morelli, E.; Spolenak, R. Fused filament fabrication of stainless steel structures-from binder development to sintered properties. *Addit. Manuf.* **2022**, *49*, 102472. [CrossRef]
13. Nocheseda, C.J.C.; Liza, F.P.; Collera, A.K.M.; Caldona, E.B.; Advincula, R.C. 3D printing of metals using biodegradable cellulose hydrogel inks. *Addit. Manuf.* **2021**, *48*, 102380. [CrossRef]
14. Venkataraman, N.; Rangarajan, S.; Matthewson, M.J.; Safari, A.; Danforth, S.C.; Yardimci, A. Mechanical and Rheological Properties of Feedstock Material for Fused Deposition of Ceramics and Metals (FDC and FDMet) and Their Relationship to Process Performance. In Proceedings of the 1999 International Solid Freeform Fabrication Symposium Proceedings, Austin, TX, USA, 9–11 August 1999; pp. 351–359. [CrossRef]
15. Gotman, I. *Characteristics of Materials Used in Implants: Metals, Stenting the Urinary System*, 2nd ed.; Informa Healthcare: London, UK, 2011; p. 61. ISBN 9781841843872.
16. Wang, Y.M.; Voisin, T.; McKeown, J.T.; Ye, J.; Calta, N.P.; Li, Z.; Zeng, Z.; Zhang, Y.; Chen, W.; Roehling, T.T. Additively manufactured hierarchical stainless steels with high strength and ductility. *Nat. Mater.* **2018**, *17*, 63–70. [CrossRef] [PubMed]
17. Sadaf, M.; Bragaglia, M.; Nanni, F. A simple route for additive manufacturing of 316L stainless steel via Fused Filament Fabrication. *J. Manuf. Process.* **2021**, *67*, 141–150. [CrossRef]
18. Betts, J.L.; Sampson, B.J.; Lindsey, K.; Brinkley, F.M.; Priddy, M.W. Reduction of Process Induced Porosity for Ultrafuse 316L through Parameter Optimization of Creality Ender 3 V2 and Makerbot Method, X. *Crystals* **2024**, *14*, 285. [CrossRef]
19. Moritzer, E.; Elsner, C.L.; Schumacher, C. Investigation of metal-polymer composites manufactured by fused deposition modeling with regard to process parameters. *Polym. Compos.* **2021**, *42*, 6065–6079. [CrossRef]
20. Dayue Jiang, D.; Ning, F. Anisotropic deformation of 316L stainless steel overhang structures built by material extrusion based additive manufacturing. *Addit. Manuf.* **2022**, *50*, 102545. [CrossRef]
21. Quarto, M.; Carminati, M.; D'Urso, G. Density and shrinkage evaluation of AISI 316L parts printed via FDM process. *Mater. Manuf. Process.* **2021**, *36*, 1535–1543. [CrossRef]
22. Thompson, Y.; Gonzalez-Gutierrez, J.; Kukla, K.; Felfer, P. Fused filament fabrication, debinding and sintering as a low cost additive manufacturing method of 316L stainless steel. *Addit. Manuf.* **2019**, *30*, 100861. [CrossRef]
23. Tosto, C.; Tirillò, J.; Sarasini, F.; Sergi, C.; Cicala, G. Fused Deposition Modeling Parameter Optimization for Cost-Effective Metal Part Printing. *Polymers* **2022**, *14*, 3264. [CrossRef]
24. Liu, B.; Wang, Y.; Lin, Z.; Zhang, T. Creating metal parts by Fused Deposition Modeling and Sintering. *Mater. Lett.* **2020**, *263*, 127252. [CrossRef]
25. Damon, J.; Dietrich, S.; Gorantla, S.; Popp, U.; Okolo, B.; Schulze, V. Process porosity and mechanical performance of fused filament fabricated 316L stainless steel. *Rapid Prototyp. J.* **2019**, *25*, 1319–1327. [CrossRef]
26. Wang, C.; Mai, W.; Shi, Q.; Liu, Z.; Pan, Q.; Peng, J. Effect of Printing Parameters on Mechanical Properties and Dimensional Accuracy of 316L Stainless Steel Fabricated by Fused Filament Fabrication. *J. Mater. Eng. Perform.* **2023**, *1*, 1–13. [CrossRef]
27. Ait-Mansour, I.; Kretzschmar, N.; Chekurov, S.; Salmi, M.; Rech, J. Design-dependent shrinkage compensation modeling and mechanical property targeting of metal FFF. *Prog. Addit. Manuf.* **2020**, *5*, 51–57. [CrossRef]
28. Kasha, A.; Obadimu, S.O.; Kourousis, K.I. Flexural characteristics of material extrusion steel 316L: Influence of manufacturing parameters. *Addit. Manuf. Lett.* **2022**, *3*, 100087. [CrossRef]
29. Carminati, M.; Quarto, M.; D'urso, G.; Giardini, C.; Maccarini, G. Mechanical Characterization of AISI 316L Samples Printed Using Material Extrusion. *Appl. Sci.* **2022**, *12*, 1433. [CrossRef]
30. Spiller, S.; Kolstad, S.O.; Razavi, N. Fabrication and characterization of 316L stainless steel components printed with material extrusion additive manufacturing. *Procedia Struct. Integr.* **2022**, *42*, 1239–1248. [CrossRef]
31. Safka, J.; Ackermann, M.; Machacek, J.; Seidl, M.; Vele, F.; Truxova, V. Fabrication process and basic material properties of the BASF Ultrafuse 316LX material. *MM Sci. J.* **2020**, *5*, 4216–4222. [CrossRef]
32. Piscopo, G.; Iuliano, L. Evaluating the Effect of Deposition Strategy on Mechanical Characteristics of 316L Parts Produced by Laser Powder Directed Energy Deposition Process. *Lasers Manuf. Mater. Process.* **2024**, *11*, 419–436. [CrossRef]
33. Nie, H.; Liu, H.; Wang, C.; Wu, Y.; Zhu, S.; Luo, J. A new laser remelting strategy for direct energy deposition of 316L stainless steel. Proceedings of the Institution of Mechanical Engineers. *Part B J. Eng. Manuf.* **2024**. [CrossRef]
34. Huang, R.; Wu, Y.; Huang, L.; Pan, C.; Sun, Y.; Tian, S.; Wang, D.; Yang, Y. Scanning strategies for the 316L part with lattice structures fabricated by selective laser melting. *Int. J. Adv. Manuf. Technol.* **2024**, *133*, 3165–3178. [CrossRef]
35. Lee, G.; Jeong, S.G.; Kwon, J.; Ahn, S.Y.; SaGong, M.J.; Lee, K.-A.; Kim, H.S. Shear deformation behavior of additively manufactured 316L stainless steel lattice structures. *Addit. Manuf.* **2024**, *93*, 104425. [CrossRef]
36. Suryawanshi, J.; Prashanth, K.G.; Ramamurty, U. Mechanical behavior of selective laser melted 316L stainless steel. *Mater. Sci. Eng.* **2017**, *696*, 113–121. [CrossRef]

37. Gong, H.; Snelling, D.; Kardel, K.; Carrano, A. Comparison of Stainless Steel 316L Parts Made by FDM- and SLM-Based Additive Manufacturing Processes. *Miner. Met. Mater. Soc.* **2019**, *71*, 880–885. [CrossRef]
38. Kedziora, S.; Decker, T.; Museyibov, E.; Morbach, J.; Hohmann, S.; Huwer, A.; Wahl, M. Strength Properties of 316L and 17-4 PH Stainless Steel Produced with Additive Manufacturing. *Materials* **2022**, *15*, 6278. [CrossRef]
39. Tosto, C.; Tirillò, J.; Sarasini, F.; Cicala, G. Hybrid metal/polymer filaments for fused filament fabrication (FFF) to print metal parts. *Appl. Sci.* **2021**, *11*, 1444. [CrossRef]
40. Naleway, S.E.; Porter, M.M.; McKittrick, J.; Meyers, M.A. Structural Design Elements in Biological Materials: Application to Bioinspiration. *Adv. Mater.* **2015**, *27*, 5455–5476. [CrossRef]
41. Natarajan, B.; Gilman, J.W. Bioinspired Bouligand cellulose nanocrystal composites: A review of mechanical properties. *Philos. Trans. R. Soc. A Math. Phys. Eng. Sci.* **2018**, *376*, 20170050. [CrossRef]
42. Zimmermann, E.A.; Gludovatz, B.; Schaible, E.; Dave, N.K.N.; Yang, W.; Meyers, M.A.; Ritchie, R.O. Mechanical adaptability of the Bouligand-type structure in natural dermal armour. *Nat. Commun.* **2018**, *4*, 2634. [CrossRef]
43. Weaver, J.C.; Milliron, G.W.; Miserez, A.; Evans-Lutterodt, K.; Herrera, S.; Gallana, I.; Mershon, W.J.; Swanson, B.; Zavattieri, P.; DiMasi, E.; et al. The stomatopod dactyl club: A formidable damage-tolerant biological hammer. *Science* **2012**, *336*, 1275–1280. [CrossRef]
44. Chen, P.Y.; Lin, A.Y.-M.; McKittrick, J.; Meyers, M.A. Structure and mechanical properties of crab exoskeletons. *Acta Biomater.* **2008**, *4*, 587–596. [CrossRef]
45. Bouligand, Y. Twisted fibrous arrangements in biological materials and cholesteric mesophases. *Tissue Cell* **1972**, *4*, 189–217. [CrossRef] [PubMed]
46. Raabe, D.; Romano, P.; Sachs, C.; Fabritius, H.; Al-Sawalmih, A.; Yi, S.-B.; Servos, G.; Hartwig, H.G. Microstructure and crystallographic texture of the chitin-protein network in the biological composite material of the exoskeleton of the lobster Homarus americanus. *Mater. Sci. Eng. A* **2006**, *421*, 143–153. [CrossRef]
47. Technical Data Sheet. Website BASF. Available online: https://forward-am.com/material-portfolio/ultrafuse-filaments-for-fused-filaments-fabrication-fff/metal-filaments/ultrafuse-316l (accessed on 5 March 2024).
48. Ultrafuse Metal Filaments. Users Guideline. BASF. Available online: https://move.forward-am.com/hubfs/AES%20Documentation/Metal%20Filaments/Ultrafuse_metal_User_Guideline.pdf (accessed on 11 November 2024).
49. *DIN EN ISO 6892-1:2019*; Metallic Materials—Tensile Testing—Part 1: Method of Test at Room Temperature. Beuth: Berlin, Germany, 2019.
50. Golod, V.; Sufiiarov, V. The evolution of structural and chemical heterogeneity during rapid solidification at gas atomization. *IOP Conf. Ser. Mater. Sci. Eng.* **2017**, *192*, 012009. [CrossRef]
51. Miyanaji, H. Binder Jetting Additive Manufacturing Process Fundamentals and the Resultant Influences on Part Quality. Ph.D. Thesis, University of Louisville, Louisville, KY, USA, 2018. [CrossRef]
52. Sufiyarov, V.; Popovich, A.; Borisov, E.; Polozov, I. Evolution of structure and properties of heat-resistant nickel alloy after selective laser melting; hot isostatic pressing and heat treatment. *Tsvetnye Met.* **2017**, *1*, 77–82. [CrossRef]
53. Rodrigues, T.A.; Escobar, J.D.; Shen, J.; Duarte, V.R.; Ribamar, G.G.; Avila, J.A.; Maawad, E.; Schell, N.; Santos, T.G.; Oliveira, J.P. Effect of heat treatments on 316 stainless steel parts fabricated by wire and arc additive manufacturing: Microstructure and synchrotron X-ray diffraction analysis. *Addit. Manuf.* **2021**, *48*, 102428. [CrossRef]
54. Wang, Y.; Zhang, L.; Li, X.; Yan, Z. On hot isostatic pressing sintering of fused filament fabricated 316L stainless steel–Evaluation of microstructure, porosity, and tensile properties. *Mater. Lett.* **2021**, *296*, 129854. [CrossRef]